Conf-9208142--3

Received SEP 2

ANL/CP--76108

DE92 041122

Time-Resolved Electron-Beam Characterizations with Optical Transition Radiation*

by

Alex H. Lumpkin
Advanced Photon Source
Argonne National Laboratory
9700 S. Cass Avenue - Bldg. 362
Argonne, Illinois 60439 USA
Phone: (708) 252-4879
FAX: (708) 252-7187

Mark D. Wilke
Physics Division
Los Alamos National Laboratory
Los Alamos, New Mexico 87545 USA

*Work supported by the U.S. Department of Energy, Office of Basic Energy Sciences, under contract No. W-31-109-ENG-38 and by the Strategic Defense Command under the auspices of the U.S. Department of Energy at Los Alamos National Laboratory.

Time-Resolved Electron-Beam Characterizations with Optical Transition Radiation*

Alex H. Lumpkin
Advanced Photon Source
Argonne National Laboratory
Argonne, Illinois 60439 USA

Mark D. Wilke
Physics Division
Los Alamos National Laboratory
Los Alamos, New Mexico 87545 USA

Abstract

Time-resolved characterizations of electron beams using optical transition radiation (OTR) as a prompt conversion mechanism have recently been extended on the Los Alamos Free-electron Laser (FEL) facility 40-MeV linac. Two key timescales for rf-linac driven FELs are the micropulse (10 ps) and the macropulse (5 μs to 1 ms). In the past we have used gated, intensified cameras to select a single or few micropulses (25 to 400 ns gate width) out of the pulse train to evaluate submacropulse effects. Recently, we have obtained some of the first measurements of micropulse bunch length (7 to 10 ps) and submacropulse spatial position and profile using OTR and a Hamamatsu streak camera. Additionally, micropulse elongation effects and head-to-tail transverse kicks are reported as a function of charge.

*Work supported by the U.S. Department of Energy, Office of Basic Energy Sciences, under contract No. W-31-109-ENG-38 and by the Strategic Defense Command under the auspices of the U.S. Department of Energy at Los Alamos National Laboratory.

1. Introduction

The continuing development of electron-beam diagnostics on the Los Alamos photo-injected, rf-linac driven Free-electron Laser (FEL) facility has recently involved the extension of our time-resolved electron beam characterizations using optical transition radiation (OTR) [1,2]. In the past in this facility we have used gated, intensified cameras to select a single or a few micropulses (25 or 400 ns gate times) out of 100's to evaluate submacropulse spot size or energy effects [3,4]. Typically, for the higher peak current (>100 A) beams, we have observed beam size or energy spread blurring if we integrated over a 100-μs long macropulse. Because OTR is a prompt mechanism compared to 10 ps, it is applicable to submicropulse phenomena (Δt, profile) as well. Because OTR is not highly efficient, it has been difficult to obtain single micropulse streak data without significant photon statistic problems. We have attacked the statistics problem by employing the synchroscan option in our streak camera mainframe to synchronously sum about 200 to 400 micropulses. For the submacropulse measurements, the slow sweep plugin was installed and its sweep time adjusted to span the macropulse length (20 μs). In this way the x-center and x-profile were followed throughout the macropulse with about 200-ns resolution (individual micropulses were not seen at this sweep speed since they were 46 ns apart). The same techniques could be applied to an energy dispersive region in the beam transport. These demonstrations extend the utility of OTR-based beam diagnostics.

2. Experimental Background and Procedures

The basic beamline design has been described previously [5] but since much of the beamline is actually in place now it is appropriate to show that configuration in Fig. 1.

Following the 6-MeV photo injector accelerator tank, there are three more accelerators (B,C,D) that combine to provide total beam energy acceleration capability to 35-40 MeV. The nominal pulse structure is a 20-μs long pulse train consisting of ~10-ps long micropulses spaced 46.3 ns apart. Micropulse charges from 0.6 to 5 nc were used. There is a single OTR profile monitor after each accelerator tank except at station 4 after tank D. Here, we have installed a two-foil OTR interferometer with a 0.8 μm thick, Al first foil followed by an aluminized(~5000 Å layer) fused-silica substrate (0.25 mm thick). The first foil is opaque to visible light and the back of the second foil was aquadagged to block Cherenkov radiation contributions. The two thirty-degree dipole bends provide the means to inject the electron beam into the resonator. In this paper, we concentrate on the diagnostics arranged around the first bend area as shown in Fig. 2. A quartz window on the zero-degree port is used for alignment access and to allow viewing the back of screen 4. There is also a port at 15° to image the beam at the middle of the bend using synchrotron radiation.

As a brief review, OTR is generated at the interface of media with different dielectric constants [1,2]. As schematically shown in Fig. 3, there are both forward lobes and backward lobes of radiation with an opening angle of $\pm 1/\gamma$, where γ is the Lorentz factor. The backward lobe angular distribution depends on the Fresnel reflection coefficients so that light exits at 90° to the beam for a 45° orientation. The mechanism might be viewed simplistically as the "instantaneous" collapse of an electric dipole when the electron in vacuum reaches the surface image charge in the medium it has been approaching (or exiting). Since it is a surface or transition boundary phenomenon, the effective spatial resolution is

excellent and the mechanism's vacuum formation time should be in the picosecond domain for 10-to-50-MeV beams [6].

In Fig. 2, the Hamamatsu C1587 streak camera station was set up on a lead-shielded optical table roughly parallel to the linac. An optical relay path transported the forward OTR radiation generated by the electron beams exiting the back of the OTR interferometer. This involved a turning mirror at the port, a 1-m focal length (f.l.) lens, the beam splitter, a second turning mirror, and a final 500 cm f.l. lens on the optical table. A 650-nm long pass filter was used to minimize temporal dispersion in the optical elements. For the submicropulse measurement, the synchroscan plugin was used with the high-Q tuner (M1954-10) providing only 1 ps (rms) jitter and about 4 ps (FWHM) temporal resolution. This system was tested on the Nd:YLF pulsed drive laser prior to installation in the vault. Although this camera has the dual-sweep feature that has been used to study the phase effects on linacs and drive lasers, we have not yet used it with OTR. The submacropulse measurements are done by using the slow sweep plugin in the same mainframe.

3. Results and Discussion

Experiments to date include the submacropulse x-center tracking and the micropulse bunch length determination. Additional aspects include further studies on micropulse elongation versus charge and possible transverse Wakefield phenomena.

In Fig. 4, a sample 20-μs long slow streak image is shown. The vertical axis is macropulse time and the horizontal axis is the x-spatial axis. This sweep speed's 200-ns sampling does not display the individual micropulses that are only 46 ns apart. The spot-size

is ~0.3 mm (FWHM) on a small time slice and may have a slightly different time average. The alignment laser was injected in the beamline bore and provided a reference source to assess instrumental tilt. Further data at minimum focus sizes would be useful.

A sample bunch length measurement is shown in Fig. 5. The calibration is 0.794 ps/pixel in the vertical and .0249 mm/pixel horizontally. The observed FWHM in this 4 nC case is ~14 ps. In Fig. 6 we show the results of analyzing the electron-beam bunch observed vs. micropulse charge. In the first cell of the photoinjector the rf-gradient is used to balance space charge elongation forces. In earlier studies Lumpkin et al. [7] showed the effect of changing the relative injection time of the drive laser on bunch length. The e-beam was measured using the Cherenkov mechanism. The linac laser pulse was kept at 8 ps (FWHM) as measured by an autocorrelator while the laser irradiation flux and hence electron beam charge were varied. At low enough charges, there can be rf bunching in the first cell while at larger charges the space charge forces dominate and elongation is observed. These results are qualitatively in agreement with simulations. As can be seen in Fig. 2, the synchrotron radiation port is also available to check bunch length noninterceptively.

An additional potential phenomenon in our system involved emittance degradation by beam missteering errors. Qualitatively, it has been calculated that transporting high charge microbunches off axis through the accelerator tank can result in head-to-tail transverse kicks to particles. A preliminary simulation is shown in Fig. 7. The synchroscan streak and OTR experiment were set up partly to diagnose such a problem and partly to look for submicropulse photoinjector-related effects on emittance. In Figs. 8 and 9, we clearly show

that at Q = 4 and 5 nC, few mm transport offsets can result in significant x-center kicks during the micropulse. As the beam is steered off-axis to the other side, the beam bunch tail kick flips over. Basically, the experiment was performed by deliberately steering the beam off-center by 1, 2, or 3 mm as viewed on screen 3 after tank C, and then either steering it back on center by the time it's viewed at station 4 (as in Fig. 8) or letting it remain uncorrected at station 4. In Fig. 9 the beam was still basically on center (as much as transport allows) through the first three tanks, but was steered off-axis through tank D as seen on screen 4. This was partly constrained by the field-of-view of the screen 4 beam spot camera and the streak camera. At a charge of 5 nc, the head-to-tail kicks to the beam center are larger than the spot diameter! Quantitative analysis is continuing as are more prototypic simulations. It is apparent the technique could be used to optimize steering of high peak current beams with bunch lengths in the 10-15 ps domain. This could be a critical feature for FEL development at shorter wavelengths.

Finally, another aspect of the OTR surface mechanism means the converter thickness or multiple scattering/reflection effects in fused silica can be avoided. An extended dynamic range beam halo measurement was proposed last fall to use a strip ND filter at the focal plane of a lens-coupled intensified system or, equivalently, within the optical transport to an intensified CID camera as shown in Fig. 2. This camera also was focused on the back of screen 4. By attenuating the central intense path of the beam spot source by a factor of 100, the halo region became easily measurable as shown in Fig. 10. The total image dynamic range is >1000 and halo intensities out beyond two beam radii are seen. Although the camera

could have been gated, the submacropulse test was performed by using three different macropulse lengths. No obvious change in the halo occurred.

4. Summary

In summary, we have graphically illustrated the extension of OTR-based electron beam (or positron) characterizations to the submicropulse regime and the continuous submacropulse regime with streak system techniques. The micropulse elongation effects (peak current), the head-to-tail kicks (effective emittance), and the halo effects are all critical to high performance or shorter wavelength FEL designs.

Acknowledgements

The authors acknowledge the support of Mark Schmitt and Bruce Carlsten for simulation of the micropulse head-to-tail effects. We also acknowledge Scott Apgar, Clint Webb, and Renee Feldman for diagnostics support and the APEX operations team including Pat O'Shea, Don Feldman, Tom Zaugg, Pat Schaffstall, Jim Early, Jerry Barton, Steve Bender, Nathan Okamoto, and Mike Feind for linac operations support.

References

1. V.L. Ginzburg and I.M. Frank, Sov. Phys. JETP 16 (1946) 15.

2. L. Wartski et al., J. Appl. Phys. 46 (1975) 3644.

3. A.H. Lumpkin, *Cherenkov and Transition Radiation Diagnostics for High-Energy Free-Electron Lasers*, AIAA-87-1358, presented at AIAA 19th Fluid Dynamics, Plasma Dynamics and Laser Conference, June 1987.

4. A. H. Lumpkin et al., NIM A285 (1989) 343.

5. P.G. O'Shea et al., Proceedings of the 13th International FEL Conference, Santa Fe, NM, NIM A318 (1992) 52.

6. D.W. Rule and R.B. Fiorito, *The Use of Transition Radiation as a Diagnostic for Intense Beams*, NSWCTR84-134, (July, 1984).

7. A.H. Lumpkin, B.E. Carlsten, and R.B. Feldman, NIM A304 (1991) 374.

Figure Captions

Fig. 1 A schematic of the Los Alamos FEL beamline and diagnostics locations.

Fig. 2 A schematic expanded view of the multiple diagnostic stations around the 30° bend area. These include the OTR/synchrotron streak camera, the OTR beam halo camera, and the synchrotron radiation beam spot camera.

Fig. 3 A schematic of optical transition radiation angular distribution lobes for forward and backward components.

Fig. 4 A slow-streak image of the 20-μs long electron macropulse at station 4. The vertical axis is very close to the 20-μs span and the spot size is ~0.3 mm (FWHM).

Fig. 5 A synchroscan streak image of the electron beam micropulse bunch-length. Since the instrument temporal jitter is much less than 10 ps, the 400 micropulse sum represents the single micropulse bunch length.

Fig. 6 Micropulse elongation effects in a photoinjector are displayed versus charge in a bunch.

Fig. 7 Preliminary simulations of transverse spatial kicks during an electron micropulse containing 5 nc of charge and displaced 1.5 mm off-axis through tank D.

Fig. 8 A composite of screen 3 beam spots and screen 4 streak images for steered "right", "center", and "left". Note the head-to-tail flipping at Q = 4 nc for offsets of about 3 mm at screen 3.

Fig. 9 A composite of streak images at station 4 for steering horizontally "right to left" across the scene. Note the flip of the head-to-tail kick. Time increases going down on the vertical axis.

Fig. 10 An example of a beam-halo measurement using an extended dynamic range imaging system and the OTR conversion mechanism.

Schematic of APEX
Master Oscillator Power Amplifier (MOPA)

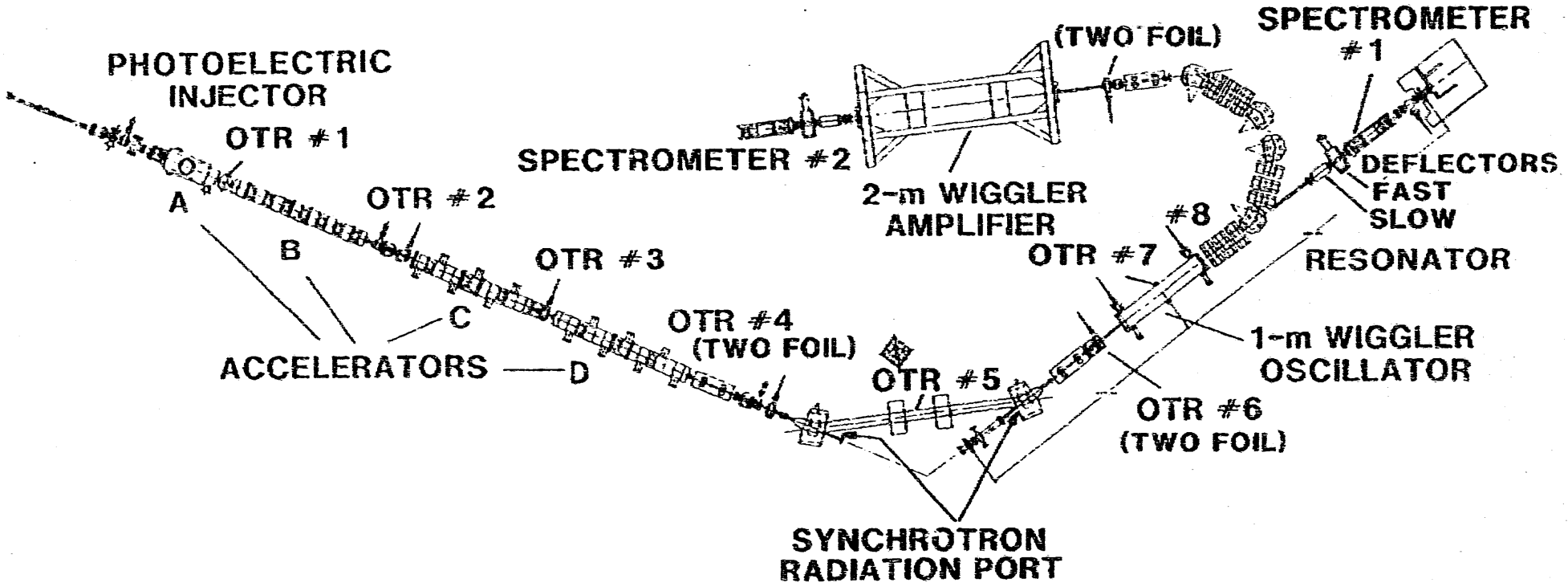

Fig. 1

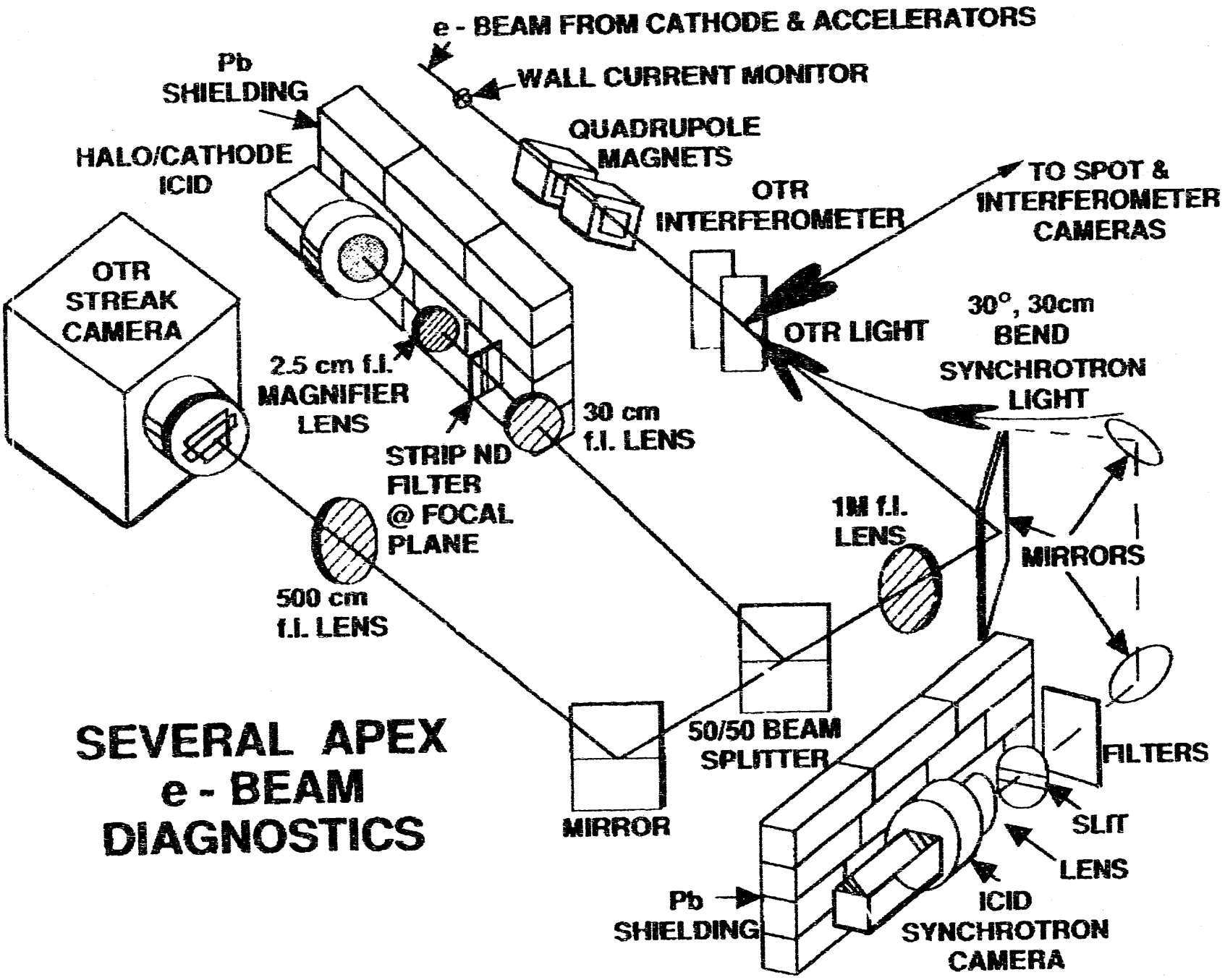
e - BEAM FROM CATHODE & ACCELERATORS
Pb SHIELDING
WALL CURRENT MONITOR
QUADRUPOLE MAGNETS
HALO/CATHODE ICID
OTR INTERFEROMETER
TO SPOT & INTERFEROMETER CAMERAS
OTR STREAK CAMERA
OTR LIGHT
30°, 30cm BEND
SYNCHROTRON LIGHT
2.5 cm f.l. MAGNIFIER LENS
30 cm f.l. LENS
STRIP ND FILTER @ FOCAL PLANE
1M f.l. LENS
MIRRORS
500 cm f.l. LENS
50/50 BEAM SPLITTER
FILTERS
MIRROR
SLIT
LENS
Pb SHIELDING
ICID SYNCHROTRON CAMERA
SEVERAL APEX e - BEAM DIAGNOSTICS

Fig. 2

OPTICAL TRANSITION RADIATION PATTERNS

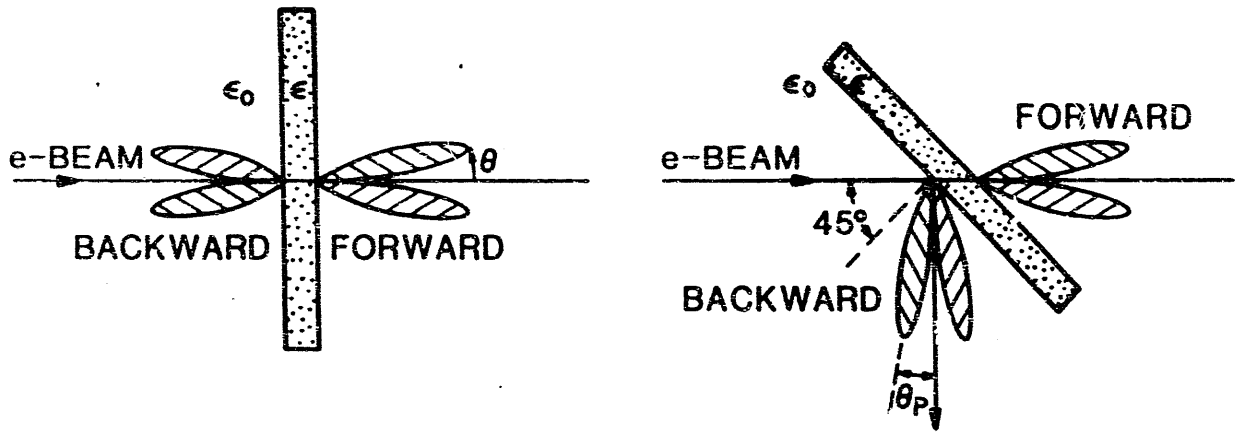

a.) NORMAL INCIDENCE

b.) OBLIQUE INCIDENCE ($\phi = 45°$)

CHERENKOV RADIATION PATTERN ($\theta \sim 46°$)

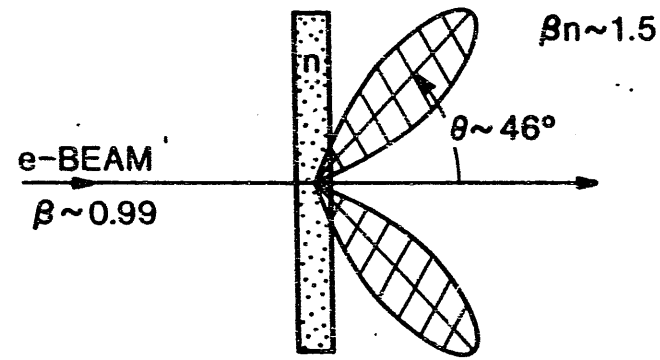

Fig. 3

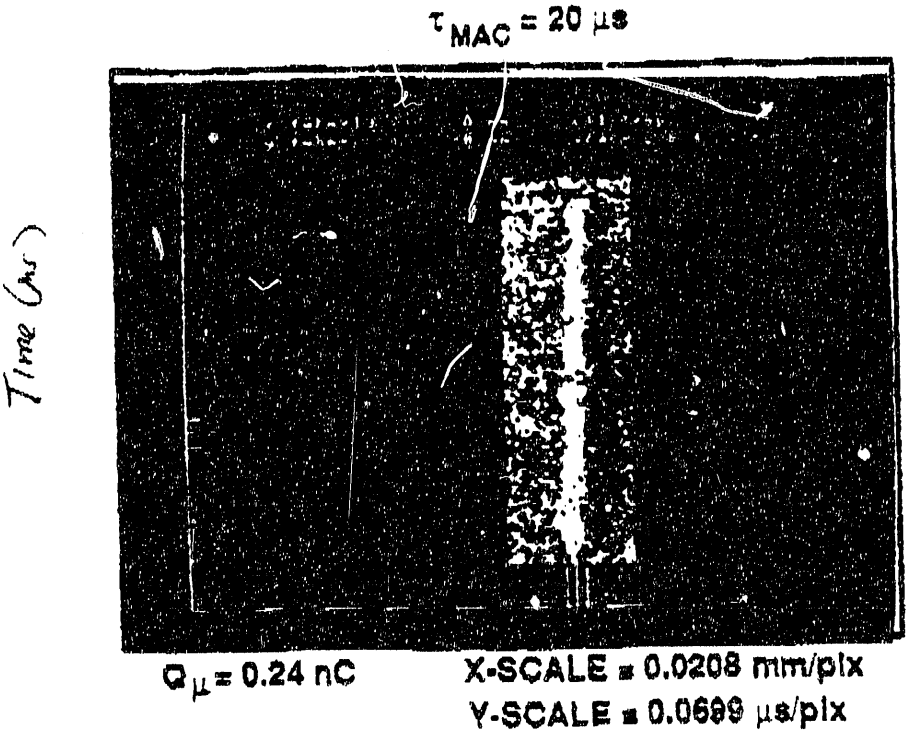
τ_{MAC} = 20 μs
Time (μs)
Q_μ = 0.24 nC
X-SCALE = 0.0208 mm/pix
Y-SCALE = 0.0699 μs/pix

Fig. 4

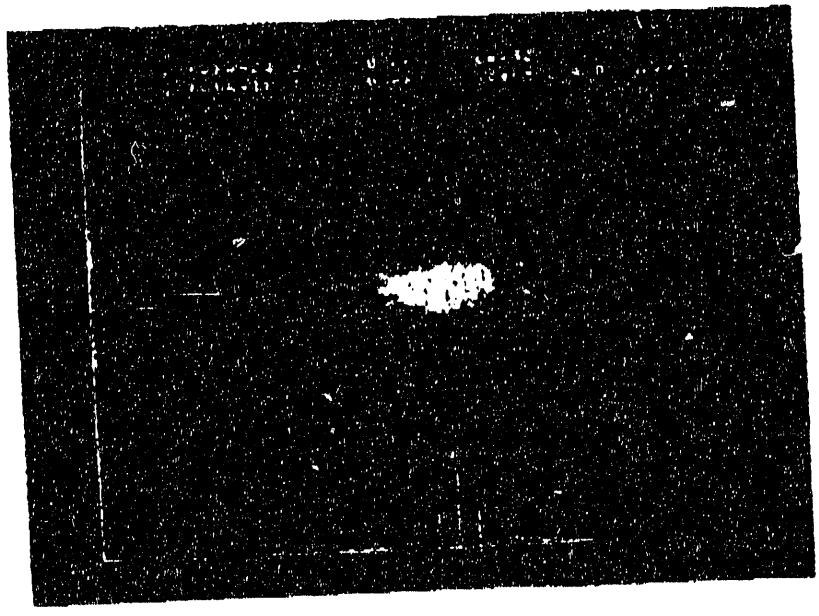

Q_μ = 4.0 nC

X-SCALE = 0.0249 mm/pix
Y-SCALE = 0.794 ps/pix

Fig. 5

MICRO PULSE LENGTH

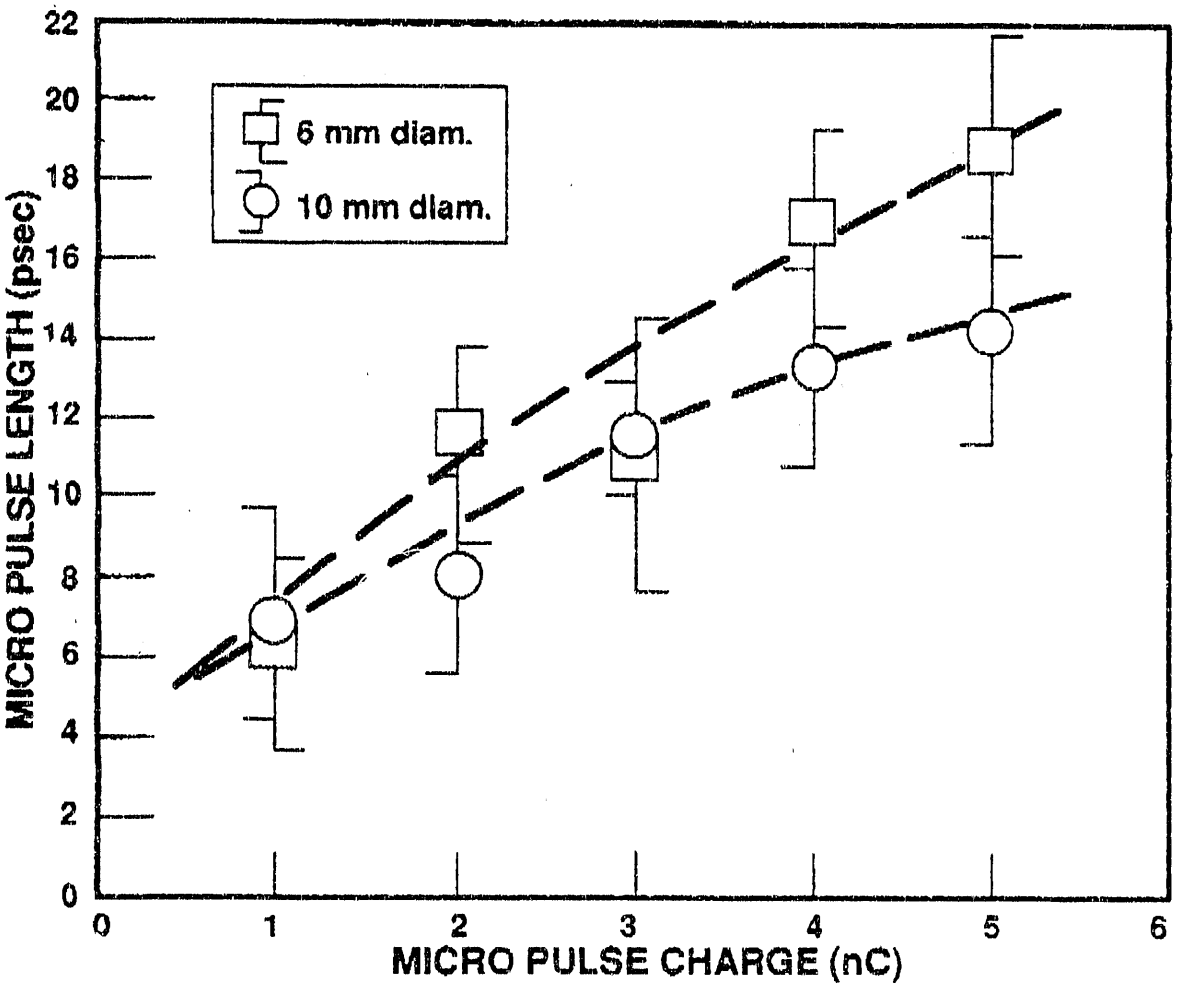

Fig. 6

TRANSVERSE WAKEFIELD EFFECTS

CLEARLY VISIBLE ON A MICROPULSE TIMESCALE

IN TANK D

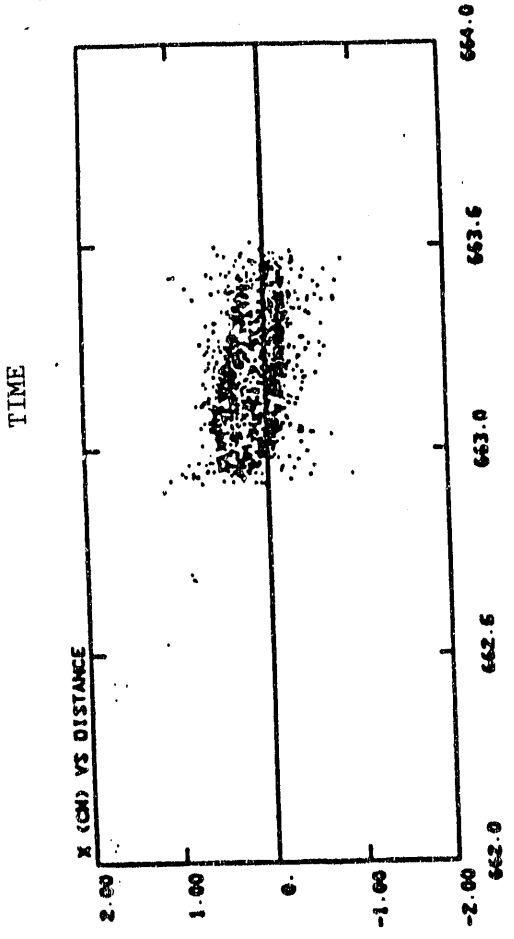

X-AXIS

FOCUS AT SCREEN 4

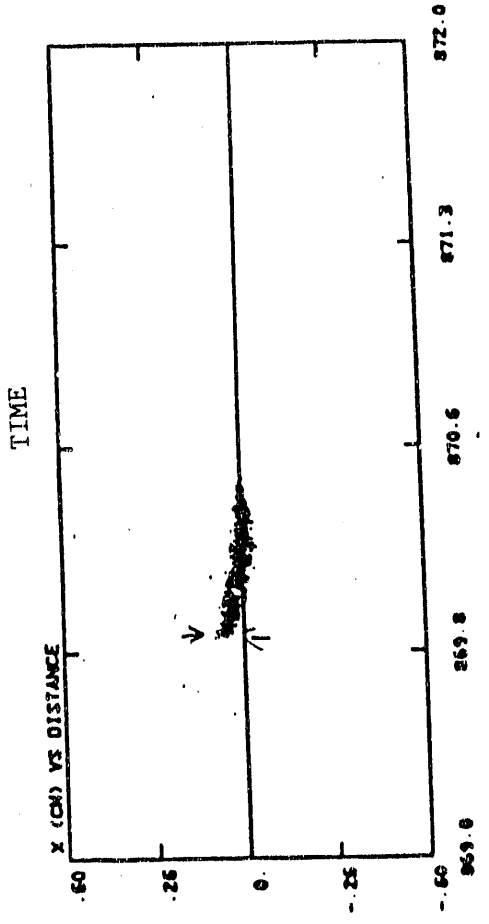

X-AXIS

Simulation by M. Schmitt
(LANL)

Fig. 7

WAKE FIELD EFFECTS

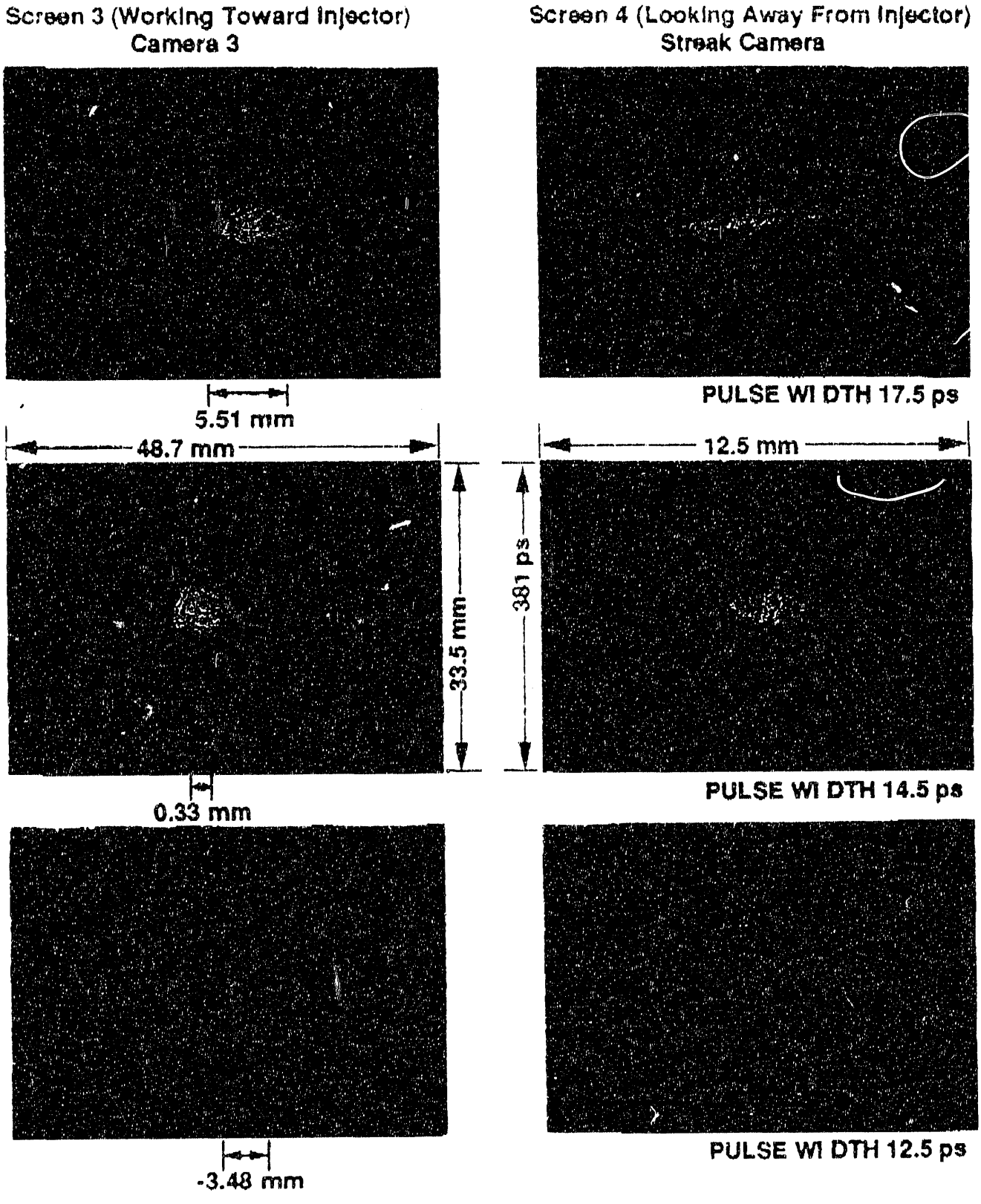

Fig. 8

WAKE OBSERVATIONS

E = 37 MeV ρ_μ = 5nC τ_M = 20 μs

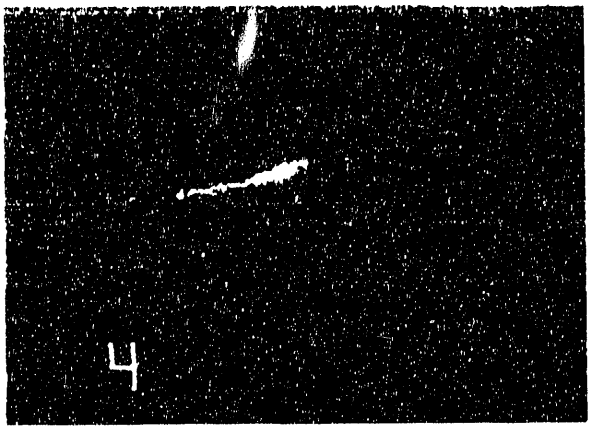

a) 1.2 mm Left @ Screen 4
FWHM x = 1.2 mm y = 27 ps

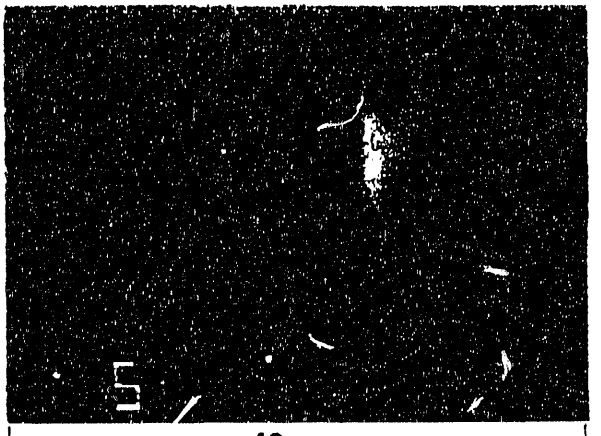

b) Screen 3 Image
FWHM x = 4.9 mm y = 8.4 mm

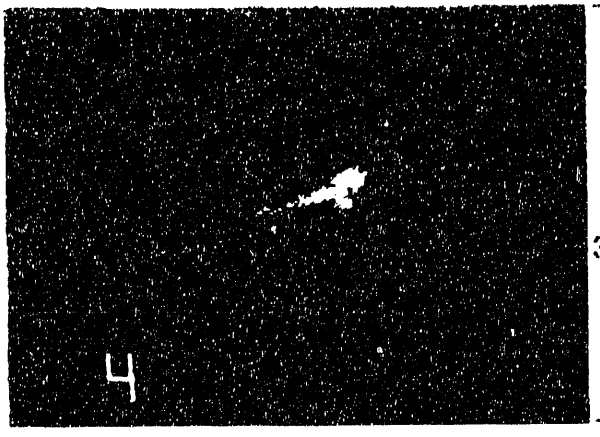

c) Centered Through Linac
FWHM x = 0.76 mm y = 26 ps

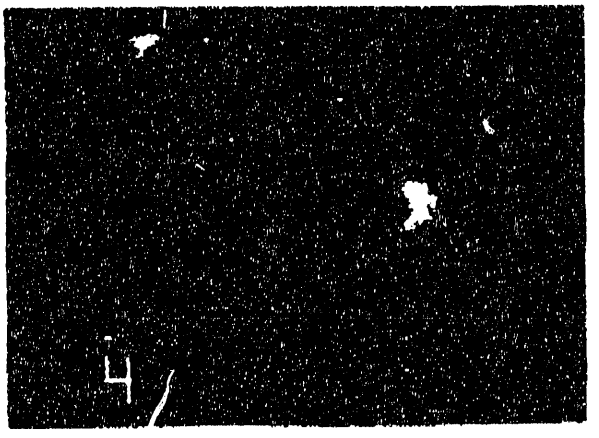

"Corrected" Position
d) 1.3 mm Right @ Screen 4
FWHM x = 0.41 mm y = 30 ps

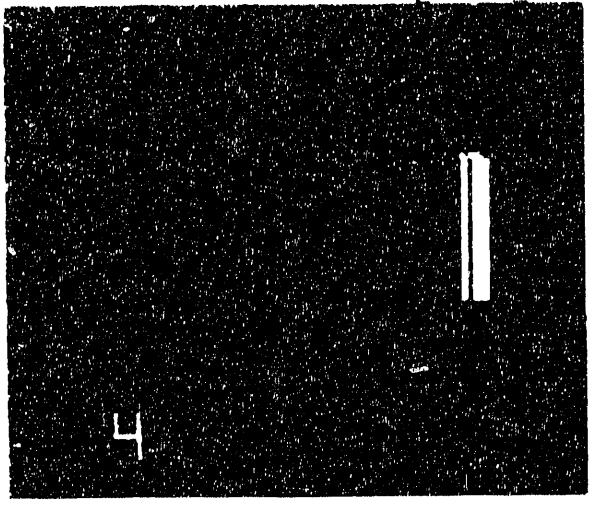

e) 1.2 mm Right @ Screen 4
FWHM x = 0.81 mm y = 27 ps

Fig. 9

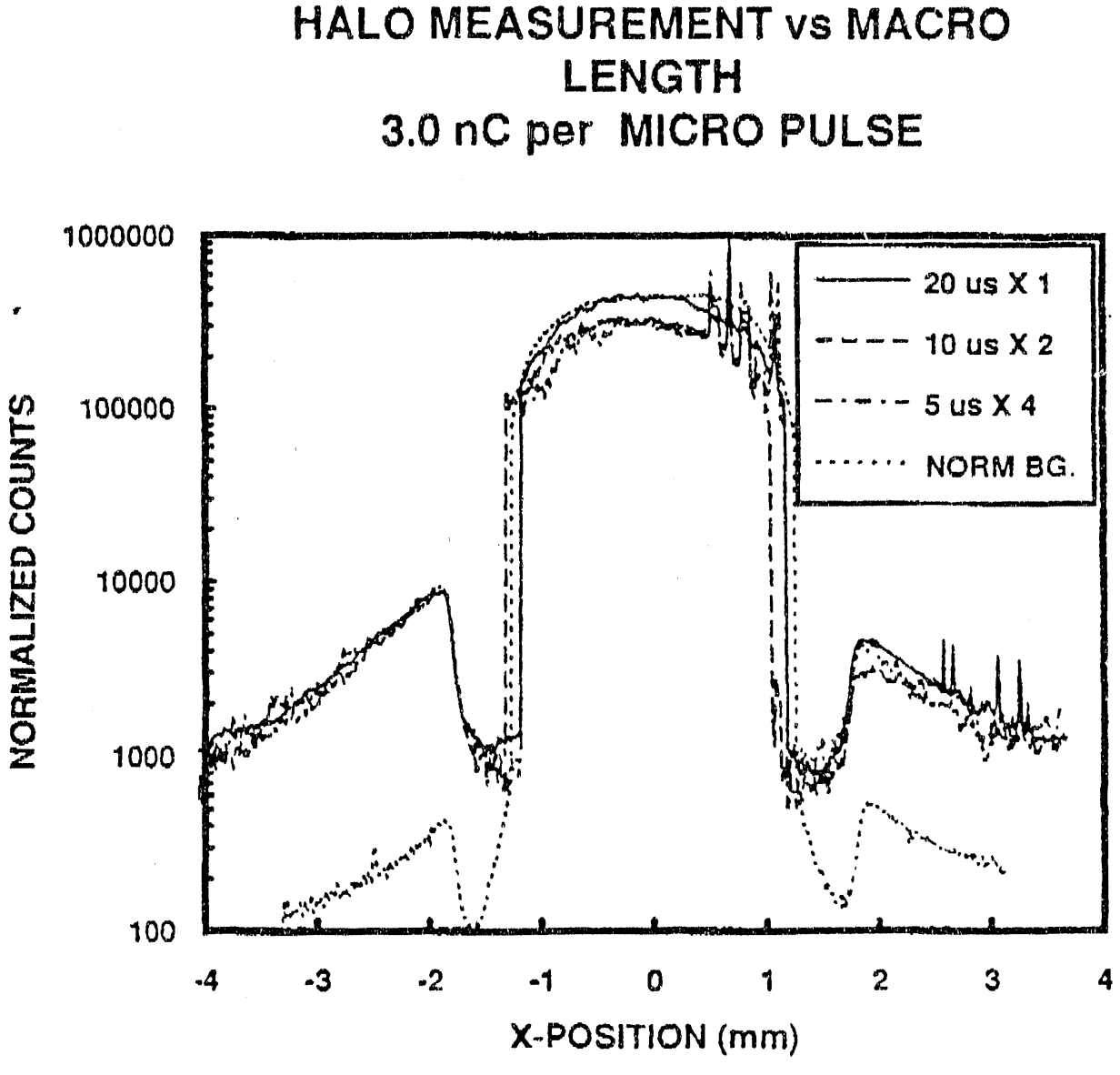
HALO MEASUREMENT vs MACRO LENGTH
3.0 nC per MICRO PULSE
NORMALIZED COUNTS
1000000
100000
10000
1000
100
-4
-3
-2
-1
0
1
2
3
4
X-POSITION (mm)
20 us X 1
10 us X 2
5 us X 4
NORM BG.

Fig. 10

END

DATE
FILMED
11/20/92